Research in Education, Technology, and Multiculture
ISSN: 3025-6763 | Journal's DOI: 10.61436/rietm
Homepage: https://imrecsjournal.com/journals/index.php/rietm

Steady RANS Assessment of Stall Fence Effects on Wells Turbine Performance for Oscillating Water Column Systems

Muhammad Nurfajriansyah Muslich[1], Aditya Rio Prabowo[1,*], Ristiyanto Adiputra[2], Seung Jun Baek[3], Svitlana Onyshchenko[4], Mahfud Alfajar[5], Dominicus Danardono Dwi Prija Tjahjana[1], Iwan Istanto[1], Rahman Wijaya[1], Hermes Carvalho[6,7]

[1]Department of Mechanical Engineering, Universitas Sebelas Maret, Indonesia
[2]Research Center for Hydrodynamic Technology, National Research and Innovation Agency, Indonesia
[3]Advanced-Green Technology Center, Korea Marine Equipment Research Institute, South Korea
[4]Department of Fleet Operation and Shipping Technology, Odesa National Maritime University, Ukraine
[5]PT. Internik Nusa Prawira, Indonesia
[6]Department of Structural Engineering, Federal University of Minas Gerais, Brazil
[7]Department of Structural Engineering and Geotechnical, University of São Paulo, Brazil

ARTICLE INFO

Article History:
Received: 09 June 2026
Accepted: 27 July 2026
Published: 04 August 2026

Keywords:
Wells turbine;
Stall fence;
CFD benchmark;
Steady RANS;
Ocean wave energy conversion.

***Corresponding Author:**
aditya@ft.uns.ac.id

ABSTRACT

The Wells turbine is a key component in an Oscillating Water Column (OWC)-based ocean wave energy conversion system, yet its limited operating range due to leading-edge stall constrains overall system efficiency. This study presents an independent CFD benchmark of the performance of the Wells turbine with and without a passive flow control device, a stall fence, as investigated by Das and Samad (2020). Steady Reynolds-Averaged Navier-Stokes (RANS) simulations using the SST k-ω turbulence model were performed in ANSYS CFX v22.1 by replicating the original geometry, boundary conditions, and mesh density for direct comparison. The reference turbine (eight NACA 0015 blades, solidity 0.64) and the configuration with a stall fence (fences at 40% and 80% span) were evaluated over a flow coefficient range of φ = 0.075-0.275. Grid independence study using quantitative (non-dimensional torque T*) and qualitative (tip-vortex topology) criteria resulted in the selection of a 3.5-million-element mesh. For the reference turbine, a mean absolute percentage error (MAPE) of 2.0% for T* and 3.1% for efficiency was obtained in the pre-stall range ($\varphi \leq 0.225$), confirming strong numerical reproducibility. However, steady RANS failed to predict the stall onset for the reference configurations and overpredicted torque by up to 508% in the post-stall region. The stall point at φ = 0.250 was successfully reproduced with a deviation approaching zero, proving that the vorticity induced by the fence geometry enhances the reliability of RANS stall predictions. The pre-stall MAPE for the fence configuration was 4.4% for T*, slightly higher due to local vortex interactions around the fence. These findings establish steady RANS as a reliable design tool in the pre-stall range and demonstrate that passive fence stalls not only extend the turbine's operating range but also improve the accuracy of CFD predictions.

To cite this article:
Muslich, M. N., Prabowo, A. R., Adiputra, R., Baek, S. J., Onyshchenko, S., Alfajar, M., Tjahjana, D. D. D. P., Istanto, I., Wijaya, R., & Carvalho, H. (2026). Steady rans assessment of stall fence effects on wells turbine performance for oscillating water column systems. *Research in Education, Technology, and Multiculture*, *5*(3), 222-238. doi: https://doi.org/10.61436/rietm/v5i3.pp222-238

■ INTRODUCTION

The continuously rising global energy demand has driven the development of sustainable, environmentally friendly renewable energy technologies. One renewable energy source with great potential that has not yet been optimally utilized is ocean wave energy. Ocean wave energy has a relatively high energy density and is continuously available in many coastal regions worldwide. One of the most widely developed conversion technologies for extracting this wave energy is the Oscillating Water Column (OWC) (Falcão & Henriques, 2016). The OWC system converts the oscillating motion of the water column induced by sea waves into a bidirectional (reciprocating) airflow within the chamber. This airflow is then converted into

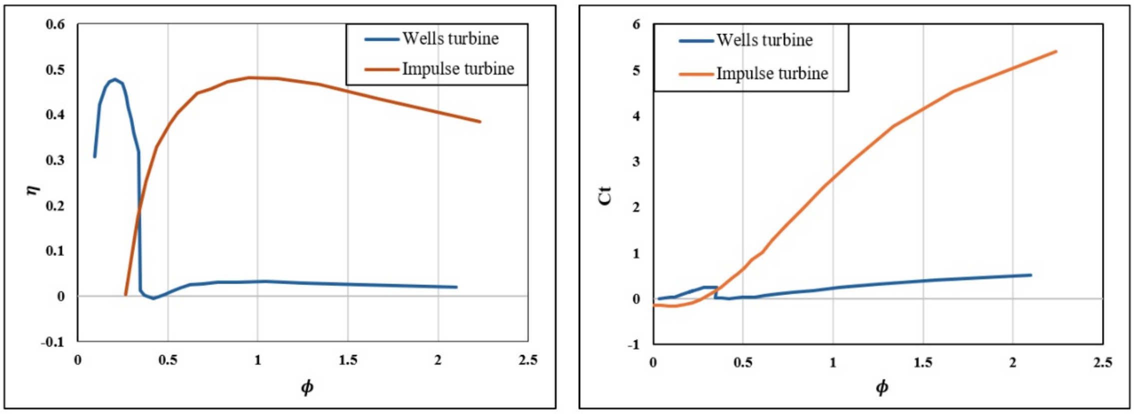

Note. Panel (a) displays efficiency (η) and panel (b) displays torque coefficient (Ct) as a function of flow coefficient (φ) for the Wells turbine and impulse turbine operating under steady-flow conditions. Adapted from "Wells Turbine for Wave Energy Conversion Improvement of the Performance by Means of Impulse Turbine for Bi-Directional Flow," by Okuhara et al. (2013), Open Journal of Fluid Dynamics, 3(2A), p. 38 (https://doi.org/10.4236/ojfd.2013.32A006). Copyright 2013 by the authors. Adapted with permission.

Figure 1. Steady-flow turbine characteristics for wells turbine and impulse turbine.

mechanical and electrical energy through a Power Take-Off (PTO) system, in which the Wells turbine is among the most widely used turbine types. The Wells turbine has a self-rectifying characteristic, enabling it to rotate in a single direction even when subjected to bidirectional airflow from wave oscillation. This advantage gives the Wells turbine a simple construction and makes it easy to integrate with the OWC system. However, compared with the impulse turbine, the Wells turbine generally exhibits lower efficiency under certain conditions and stalls at high flow coefficient values (Okuhara et al., 2013). Nevertheless, the Wells turbine continues to be studied to this day owing to its uniqueness and potential in the development of ocean wave energy conversion technology. Research efforts have been made to address the limited operating range of the Wells turbine by modifying the blade geometry. Takao et al. investigated the use of three-dimensional blades with spanwise-varying thickness, in which the chord length remained constant. In contrast, the blade thickness gradually increased from hub to tip (Takao et al., 2014). Experimental model testing and quasi-steady numerical analysis showed that this configuration effectively prevents flow separation on the suction surface near the blade tip, thereby improving the turbine's stall characteristics.

Halder et al. (2018) simultaneously optimized the blade geometry using a combined surrogate modeling approach, the Weighted Average Surrogate, to evaluate several designs. The optimized blade geometry increased turbine efficiency by 8%, demonstrating the potential of data-driven optimization methods for Wells turbine design. In another, more recent study, Kumar et al. (2019) proposed a combined approach integrating three simultaneous blade modifications: a radiused blade tip edge, an extended static trailing edge, and variable blade thickness. CFD analysis of this combined design showed an increase in turbine torque and operating range, with the radiused-tip treatment altering tip-leakage flow characteristics to delay stall onset. A recent study by Uddin et al. (2024) evaluated two hybrid airfoil blade designs combining NACA 0015 and 0025 profiles with a variable chord distribution along the span. As a result, efficiency peaked at 59.6% with a wider operating range than the constant-chord baseline. Collectively, these studies establish that geometric blade modification is the primary strategy for extending the operating range and improving the efficiency of Wells turbines.

A passive flow control concept adapted from swept-wing aeronautics is the stall fence. This technology consists of a spanwise barrier mounted on the blade surface to suppress chordwise boundary-layer migration and delay flow separation at the leading edge. In aircraft applications, the stall fence has demonstrated measurable improvements in lift coefficient and stall angle across various wing configurations, proving its effectiveness as a low-cost, geometry-based flow control device (Solfelt & Maple, 2008; Wauters et al., 2019). Das & Samad (2010) first applied this concept to the Wells turbine domain, placing two stall fences in the spanwise direction at 40% and 80% of the blade span measured from the hub. The fence dimensions were determined through surrogate-based optimization using a Kriging surrogate model with Latin Hypercube Sampling. As a result, the optimal fence geometry was 1.6% of the chord length for both height and thickness, and 80% of the chord length for the fence length. Steady RANS simulations with the SST k-ω turbulence model in ANSYS CFX 16.1 revealed that the fence generates a local vortex structure that re-energizes the separated boundary layer. This mechanism effectively suppresses the spanwise spreading of the leading-edge separation vortex. As a result, the stall point shifted from φ = 0.225 This mechanism effectively suppresses the spanwise spreading of the leading-edge separation vortex. As a result, the stall point shifted from φ = 0.250 in the fenced configuration, equivalent to a 16.6% extension of the operating range. A 16.7% reduction in the peak-to-average power ratio was also reported within the stall-free operating range, a favorable characteristic for grid integration of OWC systems. Internal flow analysis using streamline visualization, static pressure coefficient contours, Q-criterion isosurfaces, and circumferential velocity distributions confirmed that the fence acts as a vortex generator, drawing high-energy flow into the boundary layer and helping keep the flow attached to the surface at higher angles of attack.

Although the flow analysis and performance results presented by Das & Samad (2020) are highly detailed, no independent benchmark study has been conducted to systematically validate the reproducibility of their CFD methodology, either for the reference configuration or for the configuration with a stall fence. The original study validated its numerical results against experimental data from Curran & Gato (1997) and reported a maximum deviation of about 5% in the pre-stall region (φ= 0.225). They also acknowledged an overprediction at the stall point, a well-documented characteristic associated with the inherent limitation of steady RANS in resolving progressive leading-edge separation. It should also be noted that several recent studies using similar baseline geometries and numerical methodologies likewise reported strong agreement in the pre-stall phase, without explicitly addressing differences in accuracy between the modified and reference configurations in post-stall predictions. Furthermore, the systematic difference in stall prediction accuracy between fenced and unfenced geometries, specifically the mechanism by which the introduction of a stall fence improves the predictive reliability of the RANS framework, has not been analyzed or documented in previous research. Independent replication of CFD benchmarks in turbomachinery is essential to ensure that numerical results are not sensitive to undocumented solver settings, mesh-generation choices, or turbulence-model configurations. Without such a benchmark, the reliability of the steady RANS approach as a design aid for Wells turbines with passive flow control devices remains unconfirmed from an independent standpoint.

This study fills that gap by conducting an independent CFD benchmark of the Wells turbine investigated by Das & Samad (2020), covering both the reference and stall-fenced configurations. Steady RANS simulations were performed using the SST k-ω turbulence model in ANSYS CFX, replicating the original geometry, boundary conditions, and mesh density to enable direct comparison. The main objectives of this study are: (1) to reproduce and validate the non-dimensional torque and efficiency characteristics of both turbine configurations against the published results of Das & Samad (2020) and the experimental data of Curran & Gato (1997); (2) to quantitatively assess the accuracy of the steady-state RANS methodology in the pre-stall regime, defined as $\varphi \leq 0.225$ for the reference turbine and $\varphi \geq 0.250$ for the fenced turbine, through mean absolute percentage error analysis; (3) to document and physically explain the difference in stall prediction accuracy observed between the two configurations; (4) to establish a transparent and reproducible numerical baseline for future parametric studies involving the performance optimization of Wells turbines with passive flow control devices. The novelty of this study lies in the systematic quantification of RANS predictive accuracy across two geometrically distinct configurations: with and without a stall fence, providing insight into how geometry-induced flow disturbance affects the reliability of steady-state RANS stall predictions. To provide a focused framework for this investigation, the following research questions are addressed in this study: (1) To what extent can steady RANS simulations with the SST k-ω turbulence model independently reproduce the torque and efficiency characteristics reported by Das and Samad (2020) for both the reference and stall-fenced Wells turbine configurations, and within what quantitative error bounds does this reproducibility hold in the pre-stall operating range? (2) Does the introduction of a stall fence geometry fundamentally alter the predictive capability of steady RANS in capturing stall onset, and if so, what flow-physical mechanism accounts for the differential accuracy observed between the fenced and unfenced configurations?.

Table 1. Geometric parameters of the wells turbine and stall fence configurations

No	Parameter	Symbol	Value
1	Blade profile	-	NACA 0015
2	Number of blades	N	8
3	Chord length	c	0.125 m
4	Hub-to-tip ratio	h_r	0.67
5	Hub radius	r_h	0.200 m
6	Solidity at mid-span	S	0.64
7	Tip clearance	τ	1% of c
8	Rotational speed	ω_r	2000 rpm
Stall fence parameter (optimized)			
1	Fence height	h	1.6% of c
2	Fence thickness	t	1.6% of c
3	Fence length	l	80% of c
4	Fence positions (from hub)	-	40% and 80% span

Note. Geometric and stall fence parameters adopted from "Influence of Stall Fences on the Performance of Wells Turbine," by Das & Samad (2020), Energy, 194, Article 116864 (https://doi.org/10.1016/j.energy.2019.116864).

■ METHOD

This section describes the numerical methodology used to compare the CFD performance of the Wells turbine with and without a fence. The approach follows the method proposed by Das & Samad (2020), which includes geometry preparation, domain configuration, mesh generation, solver setup, and performance parameter definitions. The complete workflow is shown in Figure 2.

Geometry Preparation

This benchmark study uses the same turbine geometry as Das & Samad (2020), thereby enabling a direct comparison of the numerical results. The reference turbine consists of eight blades with symmetric NACA 0015 profiles, arranged at a stagger angle of 90˚, perpendicular to the axial direction. A chord length of 0.125 m, a hub-to-tip ratio of 0.67, a hub radius of 0.2 m, and a mid-span solidity of 0.64 were used. A blade tip clearance of 1% of the chord length was maintained. The detailed geometric parameters are summarized in Table 1. Two stall fences were placed along the blade span at 40% and 80% of the blade span measured from the hub. The fence geometry is defined by three parameters: length (l), height (h), and thickness (t), each expressed as a percentage of the blade chord length. The optimized dimensions h = t = 1.6%c and l = 80%c, as determined by the surrogate-based optimization of Das & Samad (2020), were directly adopted in this study. The blade profile geometry was reconstructed in Autodesk Fusion 360 using the "Airfoil Sketch from File" extension, which imports standard .dat (Selig-format) airfoil coordinate files and generates the sketch profile directly from the original coordinate points, without manual redrawing or interpolation, thereby preserving the exact blade curvature. The resulting profile sketch was then extruded/lofted according to the parameters listed in Table 1. At the same time, the stall-fence geometry was constructed parametrically using the adopted dimensions (h = t = 1.6%c, l = 80%c) at the specified spanwise locations.

Because of the rotationally repeating arrangement of the eight blades, only a single

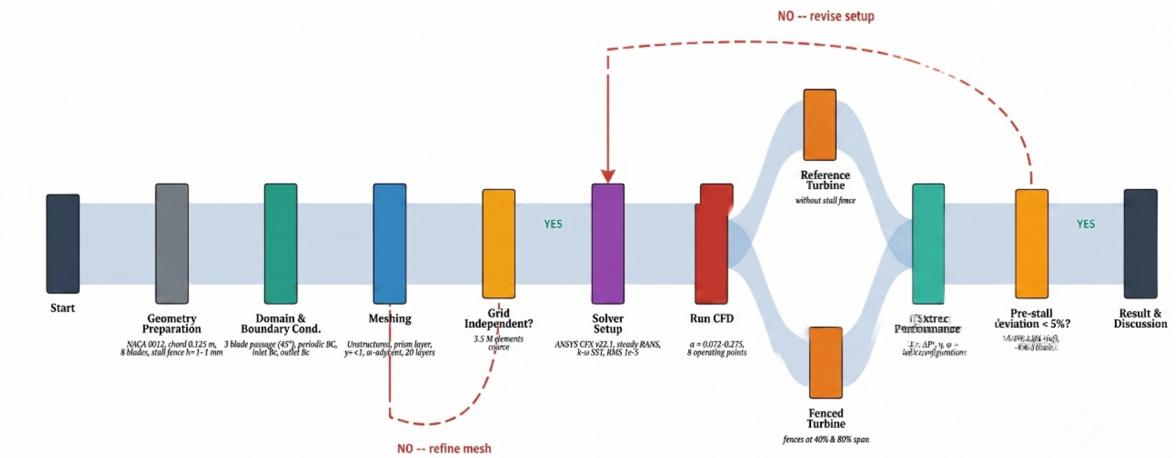

Figure 2. Methodology flowchart

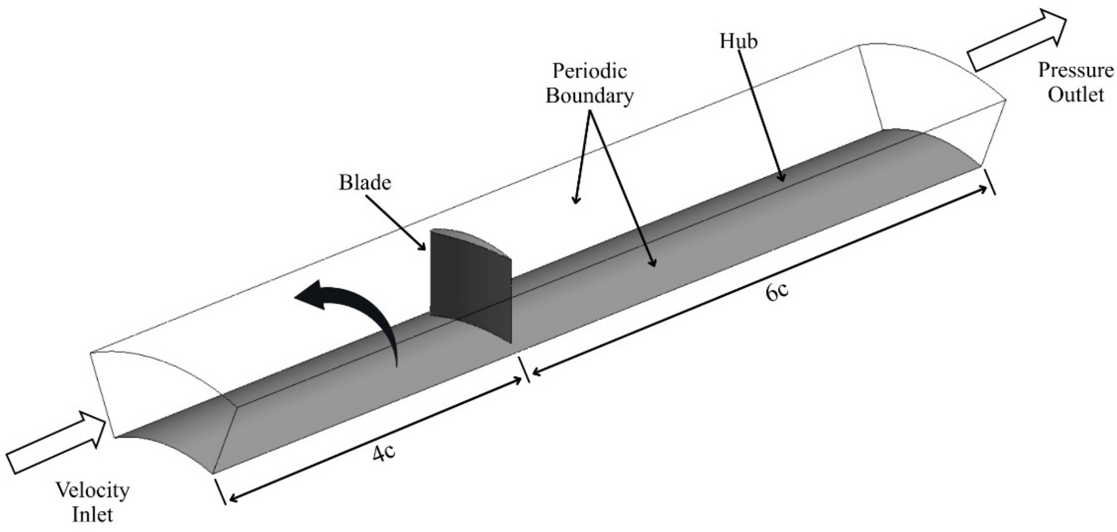

Note. The domain represents one of eight blade passages (45°) with periodic boundary conditions applied to the circumferential surfaces. Inlet and outlet channel lengths are set to 4c and 6c upstream and downstream of the rotor, respectively. Adapted from "Influence of Stall Fences on the Performance of Wells Turbine," by Das & Samad (2020), Energy, 194, Article 116864 (https://doi.org/10.1016/j.energy.2019.116864).

Figure 3. Single-passage computational domain showing boundary conditions and domain dimension

blade passage, representing 45° of the full circle, was considered the simulation domain, with periodic boundary conditions applied to its circumferential surfaces. The domain consists of a straight channel with the rotor passage at its center. An inlet channel length of four chord lengths (4c) upstream of the rotor and an outlet channel length of six chord lengths (6c) downstream were specified to ensure a fully developed inlet condition and sufficient pressure recovery at the outlet. The computational domain is shown in Figure 3. A uniform axial velocity was applied at the inlet, while ambient static pressure was specified at the outlet. At the inlet boundary, the turbulence intensity was set to 5%, and the turbulent viscosity ratio (μ_t/μ) was set to 10, consistent with high-turbulence conditions characteristic of rotating machinery flows (*ANSYS CFX-Solver Theory Guide*, 2009). The blade and hub surfaces were treated as no-slip walls. The turbine rotor rotates at a fixed speed of 2000 rpm, with the direction of rotation as defined in Figure 3. The simulations were performed at eight inlet velocities corresponding to flow coefficients φ = 0.075 to 0.275, yielding a high Reynolds number based on the relative velocity and chord length. Because the Wells turbine operates at a reduced frequency of 10^{-3} (Ghisu et al., 2018), dynamic effects can be neglected (Cambuli, 2017), and no significant performance difference is expected between steady and unsteady operating conditions (Cambuli, 2017). Therefore, only steady-state simulations were performed in this study.

Meshing

Accurate prediction of stall onset in the Wells turbine depends strongly on the resolution of the boundary-layer flow around the blade surface. Therefore, an unstructured prism layer mesh was applied in the near-wall region. An unstructured mesh was generated to discretize the computational domain. To accurately capture the boundary layer, 20 prism layers were applied normal to all blade surfaces, with the first layer set at $1.1\times10^{(-5)}$ *m* with a growth ratio of 1.2, ensuring a dimensionless wall distance of $y^+<1$ throughout. The transition from the prism layer to the bulk tetrahedral mesh was controlled using a volume change ratio of 1.5, the default value in ANSYS Meshing, which ensures a gradual size transition from the outermost prism layer element (1.3×10^{-4} *m*) to the bulk tetrahedral elements (2-3 mm in the far-field region) without abrupt jumps in element size that could introduce numerical diffusion. The resulting mesh topology around the blade and hub is shown in Figure 4. To ensure that the simulation results are independent of mesh density, a grid independence study was conducted at the flow coefficient φ= 0.225, which corresponds to the critical near-stall operating condition. Four mesh configurations were evaluated, with element counts ranging from 1.5 to 11.4 million. Two convergence criteria were applied simultaneously: (i) quantitative convergence of the non-dimensional torque T*, and (ii) qualitative convergence of the flow topology assessed

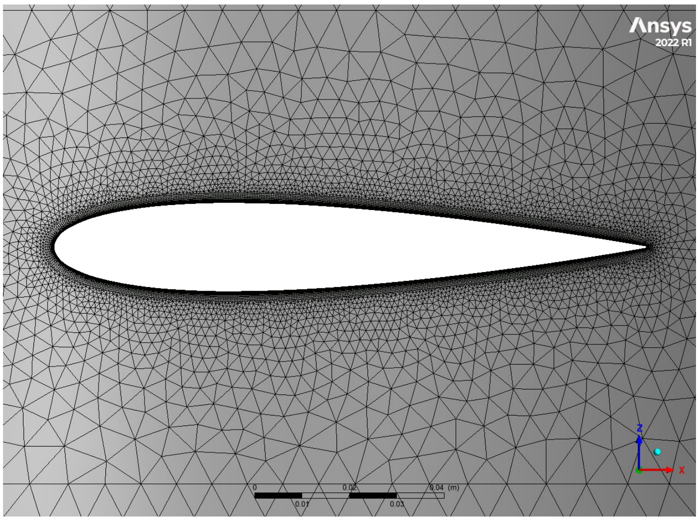

Note. *Twenty prism layers are applied normal to the blade surface with a first-layer thickness of* 1.1×10^{-5} *m and a growth ratio of 1.2, ensuring* $y^+ < 1$ *throughout. The bulk domain is discretized using an unstructured tetrahedral mesh with a volume change ratio of 1.5 at the prism-to-tetrahedral transition. Mesh generated using ANSYS Meshing 2022 R1.*

Figure 4. Unstructured mesh topology in the vicinity of the NACA 0015 Blade profile showing prism layer refinement in the near-wall region

through the streamline pattern on the blade suction side. The mesh with 3.5 million elements was selected because it met both criteria, as explained in the Results and Discussion section.

Solver Setup

The selection of the turbulence model is critical for flows involving stagnation zones and adverse pressure gradients, both of which are present at the leading edge of the Wells turbine blade and on the stall fence surface. The k-ω Shear Stress Transport (SST) model (Menter, 1993) was used in this study because it combines the k-ω formulation in the near-wall region with the k-ε model in the free stream, thereby enabling accurate resolution of both attached and separated boundary-layer flows. Previous numerical studies on Wells turbines have confirmed that the k-ω SST model provides good agreement with experimental data in the pre-stall operating range (Ghisu et al., 2018; Halder et al., 2015; Setoguchi et al., 1998). The Reynolds-Averaged Navier-Stokes (RANS) equations were solved using ANSYS CFX v22.1 (*ANSYS CFX-Solver Theory Guide*, 2009), a coupled pressure-based solver that solves the velocity and pressure fields simultaneously. A high-resolution advection scheme was applied to discretize the convective terms. In contrast, the diffusion terms were handled using the root-mean-square (RMS) residual criterion, with a threshold of 10^{-5} applied to all transport equations. Convergence was not declared based solely on the RMS residual criterion. In addition, the non-dimensional torque T was monitored as an integral quantity at each simulation point, and convergence was confirmed only when T reached a stable plateau with a variation of less than 0.1% over the final 200 iterations. This dual-criterion approach, combining residual-based and integral-quantity convergence, is consistent with best-practice recommendations for turbomachinery simulations in ANSYS CFX (*ANSYS CFX-Solver Theory Guide*, 2009) and ensures that the reported performance values correspond to a fully converged flow solution rather than a prematurely terminated iteration history.

The turbine performance is described using non-dimensional parameters to allow direct comparison with the published experimental data (Curran & Gato, 1997) and numerical data (Das & Samad, 2020). The non-dimensional torque T*, the non-dimensional pressure drop ΔP_0^*, efisiensi η, and the flow coefficient φ are defined as follows :

$$T^* = \frac{T}{\rho\,\omega^2 r\,R^5} \quad (1)$$

$$\Delta P_0^* = \frac{\Delta P_0}{\rho\,\omega^2 r\,R^2} \quad (2)$$

$$\eta = \frac{T\,\omega r}{\Delta P_0\,Q} \quad (3)$$

$$\phi = \frac{u_a}{u_t} \quad (4)$$

Where T is the total torque (*Nm*), ρ is the air density (*kg/m*³), ωr is the rotational speed (*rad/s*), R is the blade tip radius (*m*), ΔP_0 is the pressure drop across the rotor (*Pa*), Q is the volumetric flow rate (*m*³*/s*), Ua is the axial inlet velocity (*m/s*), and Ut is the blade tip velocity (*m/s*). These parameters are presented as functions of φ, where the benchmark results are compared with the experimental data of Curran and Gato (1997) and the numerical results of Das and Samad (2020).

■ RESULT AND DISCUSSION

This section presents the benchmark results for the reference turbine and the stall-fenced turbine configurations. The results are organized into six subsections: the grid independence study, validation of the reference turbine, validation of the stall-fenced turbine, differential stall prediction accuracy, physical evidence of the flow, and a discussion of the limitations of RANS. All quantitative comparisons were made against the numerical results of Das and Samad (2020) and, where applicable, the experimental data of Curran and Gato (1997).

Grid Independence Study

The grid independence study was conducted at the flow coefficient φ equals 0.225 and 0.150 using four different mesh densities ranging from 1.6 million to 11.4 million elements. Two convergence criteria were applied simultaneously: (i) quantitative convergence evaluated through the non-dimensional torque value T*, and (ii) qualitative convergence evaluated through the flow pattern on the blade suction surface in the trailing-edge region. The results are presented in Table 2.

From a quantitative standpoint, the non-dimensional torque T* remained relatively consistent across all four mesh levels, with deviations of less than 5% from the finest mesh (M4, 11.4 million elements). This pattern is consistent with the low sensitivity of integral quantities, such as rotor torque, to local mesh refinement, because the global force balance is primarily determined by the large-scale pressure distribution over the blade surface rather than by fine-scale flow structures. Although the error pattern in Table 2 is non-monotonic, with the deviation increasing from 1.19% (M2 vs. M4) to 2.84% (M3-M4), this oscillatory behavior does not invalidate the selected mesh. Grid Convergence Index (GCI) calculations were performed with Fs = 1.25 and p = 2, the nominal order of the high-resolution advection scheme, adopted because the negative sign of e_{32}/e_{21} = -0.58 prevents empirical determination of the observed order of accuracy. The GCI computed directly between the selected mesh M2 and the finest mesh M4 is 1.24%, well below the commonly accepted 3% threshold, confirming that M2 yields results that are practically equivalent to those of the finest mesh. The elevated GCI of 9.92% at the M3-M4 pair reflects a local T* overshoot at M3 (2.2414 vs. 2.1794 at M4), characteristic of oscillatory convergence at

Table 2. Grid independence study results at φ = 0.225 (near-stall) and φ = 0.150 (pre-stall)

Mesh	Elements	T*	ΔT* vs M4 %	Avg. Skewness	Avg. Aspect Ratio	Min. Orthogonal Quality	Tip Vortex Resolution	Selected
φ = 0.225 Near-stall (primary study)								
M1	1.6 million	2.2220	1.96	0.237	18.765	0.049	Not resolved	No
M2	3.5 million	2.2053	1.19	0.217	13.889	0.068	Resolved	YES
M3	7.2 million	2.2414	2.84	0.200	11.202	0.064	Resolved	-
M4	11.4 million	2.1794	(baseline)	0.196	9.336	0.063	Resolved	-
φ = 0.150 Pre-stall								
M1	1.6 million	0.9733	2.44	0.237	18.765	0.049	Not resolved	No
M2	3.5 million	0.9840	1.37	0.217	13.889	0.068	Resolved	YES
M3	7.2 million	0.9949	0.28	0.200	11.202	0.064	Resolved	-
M4	11.4 million	0.9976	(baseline)	0.196	9.336	0.063	Resolved	-

Note. T* = non-dimensional torque; ΔT* = percentage deviation of each mesh relative to the finest mesh M4 (baseline), computed as [(T*mesh - T*M4) / T**M4] × 100. GCI = Grid Convergence Index, calculated following Roache (1998) with safety factor F_s = 1.25 and nominal second-order accuracy p = 2. Convergence at φ = 0.225 is oscillatory (e_{32}/e_{21} = -0.58), confirming that non-monotonic behavior at this condition is associated with near-stall flow sensitivity rather than mesh quality degradation, as evidenced by the monotonically improving mesh quality metrics across all refinement levels. Convergence at φ = 0.150 is monotonic (e_{32}/e_{21} = +3.93). Mesh M2 was selected based on dual convergence criteria: (i) quantitative, GCI between M2 and M4 of 1.24% at φ = 0.225 and 1.43% at φ = 0.150, both within the accepted 3% threshold; and (ii) qualitative, consistent resolution of the tip-vortex topology on the blade suction surface from M2 onward, absent in M1. Mesh quality metrics (average skewness, average aspect ratio, minimum orthogonal quality) are geometric properties of the mesh and therefore identical across both flow coefficients.

intermediate refinement levels.

To verify that this oscillatory convergence pattern is a consequence of sensitivity to near-stall flow rather than a general numerical deficiency in the mesh, two complementary investigations were conducted. First, an additional grid-independence study was performed at φ = 0.150, representative of stable pre-stall operating conditions, and the results are summarised in Table 2. At this flow coefficient, convergence is strictly monotonic (e_{32}/e_{21} = +0.72), and the GCI for M2 relative to M4 is 0.50%, well within the accepted threshold and substantially lower than the 1.24% obtained at φ = 0.225. This confirms that the oscillatory behavior at φ = 0.225 is physically driven by near-stall flow instability rather than by mesh-induced numerical error. Second, mesh quality metrics were extracted for all four configurations and are reported in Table 2. The average skewness decreases monotonically from 0.237 (M1) to 0.196 (M4), and the average aspect ratio similarly improves from 18.765 to 9.336 across all mesh levels. Critically, M3 exhibits lower average skewness (0.200 vs. 0.217) and a lower average aspect ratio (11.202 vs. 13.889) than M2, demonstrating that the T* overshoot at M3 cannot be attributed to mesh-quality degradation at that refinement level. The slight increase in maximum skewness at M3 (0.877) relative to M2 (0.832) is attributable to isolated elements near the fence geometry and does not reflect a global regression in quality. Taken together, these results confirm that the oscillatory T* behavior at φ = 0.225 is a

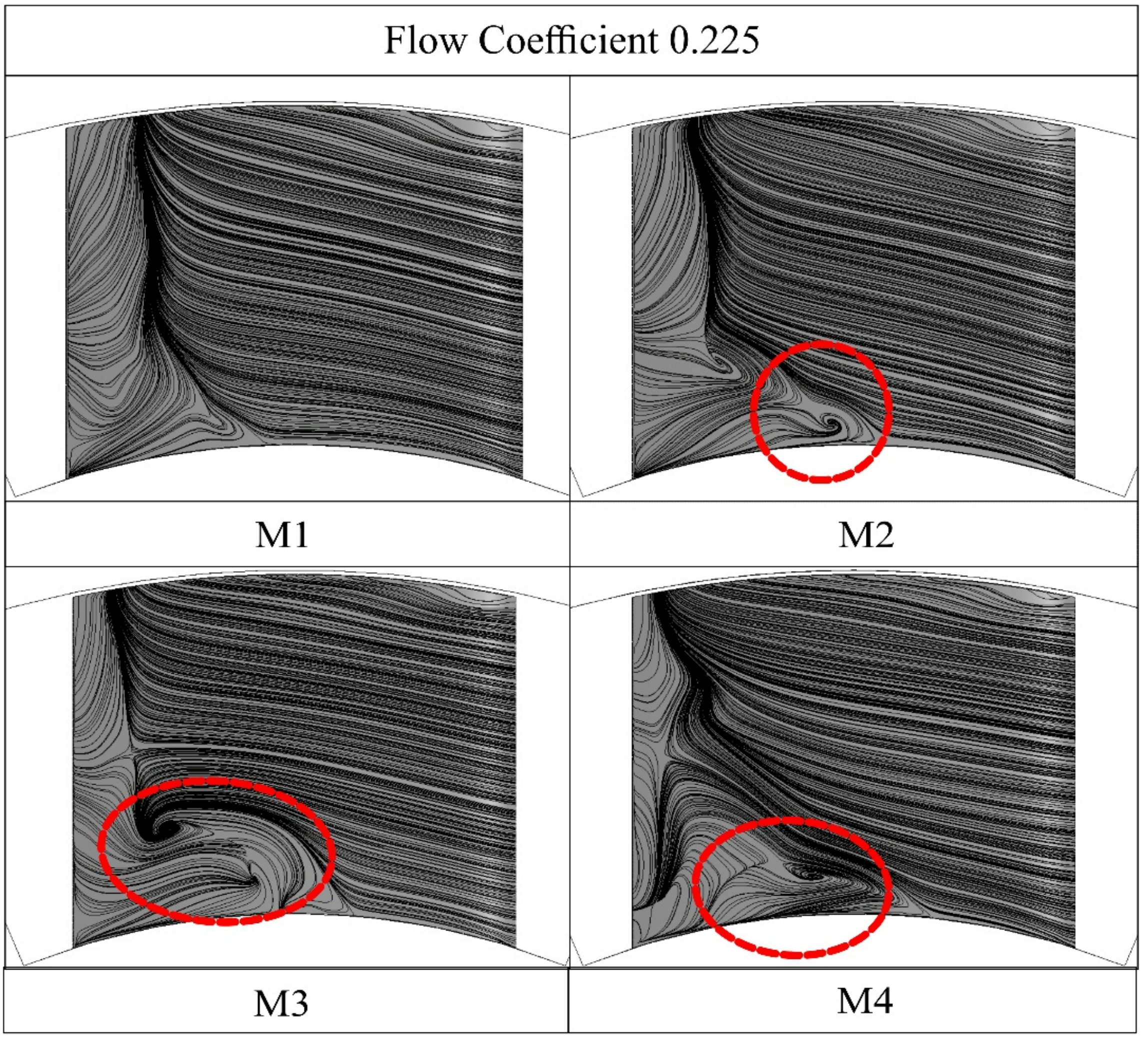

Note. Streamlines visualized on the blade suction surface at mid-span using ANSYS CFD-Post 2022 R1. Red dashed circles highlight the tip vortex structure used as the qualitative convergence criterion for mesh selection. The tip vortex is absent in M1 (1.6 million elements) but consistently resolved from M2 (3.5 million elements) onward, confirming the adequacy of M2 as the selected mesh. Flow coefficient φ = 0.225 corresponds to the critical near-stall operating condition.

Figure 5. Streamline topology on the blade suction surface for mesh configurations m1-m4 at φ = 0.225

Table 3. Quantitative comparison of t* and efficiency (η) between present benchmark and Das & Samad (2020) for the reference turbine configuration

φ	**T* Das & Samad (2020)**	**T*Present**	**Error T* (%)**	***η* Das & Samad (2020)**	***η* Present**	**Error *η* (%)**
0.075	0.010426	0.01076	+3.2	0.46914	0.47564	+1.4
0.100	0.023659	0.02414	+2.0	0.54321	0.57210	+5.3
0.125	0.040100	0.04105	+2.4	0.59012	0.59809	+1.4
0.150	0.061754	0.06046	-2.1	0.59753	0.60013	+0.4
0.175	0.083810	0.08281	-1.2	0.57531	0.59381	+3.2
0.200	0.109875	0.10697	-2.6	0.56296	0.58085	+3.2
0.225	0.135940	0.13558	-0.3	0.52593	0.56256	+7.0
0.250	0.070175	0.17022	+142.6	0.24938	0.57104	+129.0
0.275	0.031278	0.19036	+508.6	0.08642	0.52728	+510.1

Note. All values obtained from steady-state RANS simulations using the SST k-ω turbulence model in ANSYS CFX 2022 R1. T* = non-dimensional torque; η = efficiency. Error (%) = [(T*Present - T*Das & Samad) / T*Das & Samad] × 100. Positive values indicate overprediction by the present benchmark. Data for Das & Samad (2020) reproduced from Das & Samad, Energy, 194, Article 116864 (https://doi.org/10.1016/j.energy.2019.116864). Shaded rows (φ = 0.250 and φ = 0.275) indicate post-stall operating conditions where steady RANS predictive validity breaks down.

physical phenomenon associated with sensitivity to near-stall vortex structure, not a numerical artifact of deteriorating element quality.

However, the qualitative analysis of the streamline pattern on the blade suction side revealed a fundamental difference between mesh levels. The M1 mesh level (1.6 million elements) was unable to reproduce the tip vortex on the suction side, a physically significant flow structure associated with blade-tip leakage and boundary-layer interaction in Wells turbines. This vortex structure was consistently reproduced from M2 (3.5 million elements) onward. Figure 5 compares the flow topology at the four mesh levels, clearly illustrating the absence of the tip vortex at M1 and its consistent presence from M2 onward. These results show that quantitative convergence of integral performance parameters alone is insufficient as a mesh selection criterion in studies aimed at detailed flow-physics analysis. Mesh M2 was therefore selected for all subsequent simulations based on a dual convergence criterion: it satisfies the quantitative GCI threshold (1.24% < 3%) and the qualitative tip-vortex resolution criterion, while offering a computational cost (3.5 million elements) significantly lower than M3 (7.2 million elements) and M4 (11.4 million elements), consistent with standard engineering CFD practice of selecting the coarsest mesh that satisfies all convergence requirements.

These results show that the quantitative convergence of integral performance parameters alone is insufficient as a mesh selection criterion in studies aimed at detailed flow-physics analysis. Therefore, the mesh with 3.5 million elements (M2) was selected for all subsequent simulations, satisfying both quantitative convergence and qualitative flow-topology convergence while maintaining a mesh density consistent with that reported by Das & Samad (2020).

Validation of Reference Turbine

The non-dimensional torque T* and turbine efficiency η obtained from the reference turbine simulation were compared with the results published by Das & Samad (2020) and the experimental results of Curran & Gato (1997) over the entire flow coefficient range. The quantitative comparison is presented in Table 3, while the corresponding performance curves are shown in Figure 6.

In the pre-stall range between φ= 0.075 and φ= 0.225, the benchmark model shows very good agreement with the reference paper. The non-dimensional torque error varies in sign along the flow coefficient, ranging from *-2.6%* at φ= 0.20 to *+3.2%* at φ= 0.075 indicating the absence of systematic bias and confirming that the agreement reflects genuine numerical consistency rather than compensating errors. The mean absolute percentage error (MAPE) for T* over the full pre-stall range (φ= 0.075-0.225) is 2.0% and 2.2% for the strict pre-stall range (φ= 0.075-0.175). The efficiency prediction shows equally strong agreement, with MAPE values of 3.1% and 2.3%, respectively. To supplement the MAPE metric and expose point-wise deviation characteristics that a mean value may obscure, the standard deviation of the percentage error (σ) was computed across all pre-stall operating points.

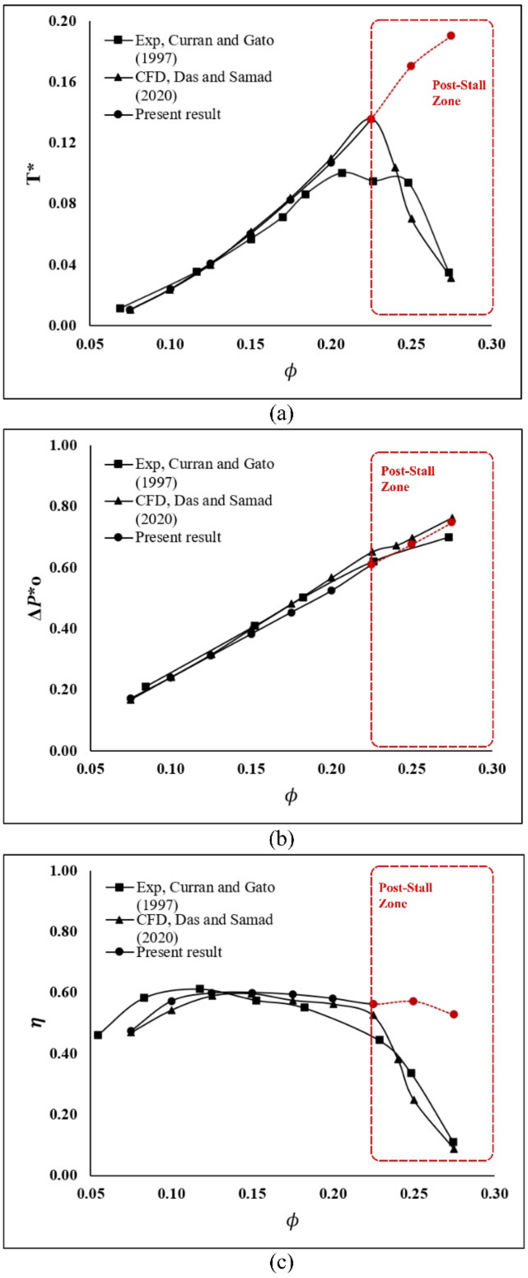

Note. The post-stall zone (φ > 0.225) is demarcated by a red dashed boundary in each panel, indicating the operating range where the predictive validity of steady RANS breaks down. Exp. = experimental data from Curran & Gato (1997); CFD Das & Samad (2020) = numerical results from Das & Samad, Energy, 194, Article 116864 (https://doi.org/10.1016/j.energy.2019.116864); Present result = present benchmark study. Experimental data adapted from "The Energy Conversion Performance of Several Types of Wells Turbine Designs," by Curran & Gato (1997), Proceedings of the Institution of Mechanical Engineers, Part A: Journal of Power and Energy, 211(2), pp. 133-145 (https://doi.org/10.1243/0957650971537051).

Figure 6. Performance curves of the reference wells turbine: (a) non-dimensional torque t*, (b) non-dimensional pressure drop δp*, and (c) efficiency η

For the full pre-stall range (φ=0.075-0.225,n=7), σ=2.3 for T*, a value commensurate with the corresponding MAPE of 2.0%, indicating a uniform error distribution without statistically dominant outliers at any single operating point. The close agreement between MAPE and σ confirms that no individual flow coefficient disproportionately influences the mean error. The benchmark consistently reproduces the reference results of Das and Samad (2020) with point-wise numerical fidelity across the entire pre-stall operating range.

The most striking agreement is observed at the numerically reported stall onset point, φ= 0.225, where the T* deviation is only 0.3%, indicating near-perfect reproduction of the turbine torque at this critical operating point. As shown in Figure 6, the benchmark curve closely matches the numerical curve of Das & Samad (2020) and the experimental data of Curran & Gato (1997) across the entire pre-stall range, thereby supporting the accuracy of the present simulation setup.

Above φ=0.225, the benchmark results deviate significantly from the reference study. At φ=0.250, the reference report *T*=0.070*, which corresponds to a deep stall condition. In contrast, the benchmark predicts *T*=0.170*, a deviation of 142.6%. A φ= 0.275, the deviation reaches 508.6%, with the benchmark maintaining *T*=0.190* compared with the reference value of 0.031. The corresponding efficiency deviations are 182.9% and 510.1%, respectively. These post-stall values are excluded from the MAPE calculation. The physical basis for this overprediction is analyzed in the Limitations of Steady RANS section.

Validation of Fenced Turbine Configuration

The non-dimensional torque and efficiency results for the stall-fenced turbine are presented in Table 4 and Figure 7. Unlike the reference turbine, the experimental dataset of Curran and Gato (1997) does not include the fenced turbine configuration. Therefore, the quantitative comparison for the fenced geometry was performed exclusively against the numerical results of Das and Samad (2020). Figure 7 presents a performance comparison with the two curves overlaid, allowing a direct visual comparison between the benchmark results and the numerical results of the reference study.

In the strict pre-stall range (φ= 0.075-0.175), the MAPE for T* is 4.4%, higher than the 2.2% achieved by the reference turbine in the same range. This higher error reflects the geometric complexity introduced by the fence structure, which generates local vortices that steady RANS resolves with slightly lower precision than for the clean reference blade. Nevertheless, the agreement remains within acceptable limits for validation. A notable anomaly is observed at φ= 0.200, where the T* error increases to 17.4% and the efficiency

Table 4. Quantitative comparison of t and efficiency (η) between present benchmark and Das & Samad (2020) for the stall-fenced turbine configuration

φ	T* Das and Samad (2020)	T*Present	Error T* (%)	η Das and Samad (2020)	η Present	Error η (%)
0.075	0.00957	0.00996	+4.2	0.44967	0.44878	-0.2
0.100	0.02087	0.02281	+9.3	0.52810	0.55140	+4.4
0.125	0.03913	0.03890	-0.6	0.58039	0.58533	+0.9
0.150	0.06261	0.05843	-6.7	0.59608	0.59138	-0.8
0.175	0.08087	0.07982	-1.3	0.56209	0.58540	+4.1
0.200	0.08609	0.10111	+17.4	0.49935	0.56001	+12.1
0.225	0.09739	0.10987	+12.8	0.44967	0.48156	+7.1
0.250	0.10348	0.12500	+20.8	0.38954	0.42387	+8.8
0.275	0.04696	0.09126	+94.4	0.13595	0.26284	+93.3

Note. All values obtained from steady-state RANS simulations using the SST k-ω turbulence model in ANSYS CFX 2022 R1. T* = non-dimensional torque; η = efficiency. Error (%) = [(*TPresent − *TDas & Samad) / *T**Das & Samad] × 100. Positive values indicate overprediction by the present benchmark; negative values indicate underprediction. Validation for the stall-fenced configuration is performed exclusively against the numerical data of Das & Samad (2020), as no experimental data are available for this geometry in the published literature. Data for Das & Samad (2020) reproduced from Das & Samad, Energy, 194, Article 116864 (https://doi.org/10.1016/j.energy.2019.116864).

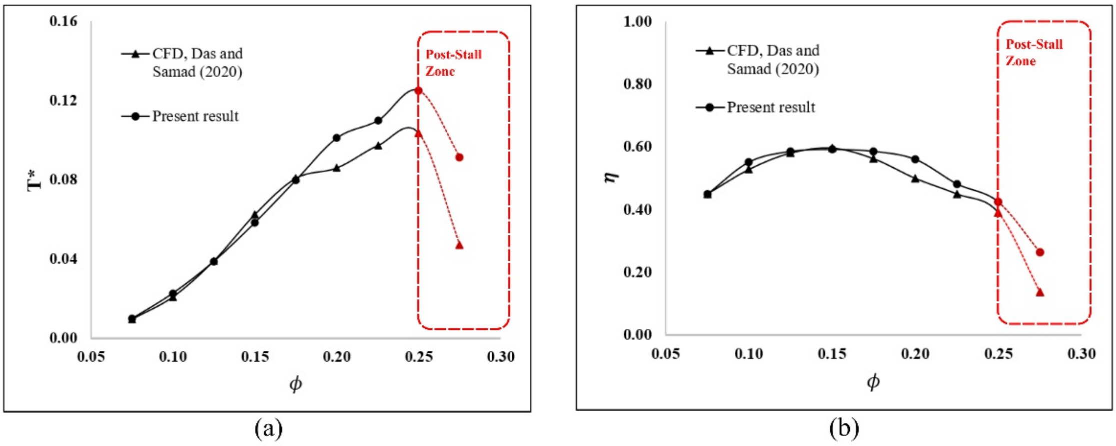

Note. The post-stall zone (φ > 0.250) is demarcated by a red dashed boundary in each panel, indicating the operating range where the predictive validity of steady RANS breaks down for the fenced configuration. CFD Das & Samad (2020) = numerical results from Das & Samad, Energy, 194, Article 116864 (https://doi.org/10.1016/j.energy.2019.116864); Present result = present benchmark study. No experimental data are available for the stall-fenced configuration; validation is performed exclusively against the numerical results of Das & Samad (2020).

Figure 7. Performance curves of the stall-fenced wells turbine: (a) non-dimensional torque t* and (b) efficiency η

error to 12.1%. This local deviation, occurring before stall onset, is consistent with the emergence of fence-induced flow disturbance. The phenomenon begins to alter the boundary-layer behavior from this flow coefficient onward, slightly earlier than the stall onset at φ= 0.225 as reported by Das and Samad (2020). This finding suggests that the effective aerodynamic influence of the fence on the RANS solver begins at φ=0.200.

Most significantly, the benchmark accurately reproduces the stall point of the fenced turbine at φ= 0.250, where T* reaches its peak and begins to decline in accordance with stall onset. The stall-point deviation is nearly zero relative to the reference results, representing the key validation finding for the fenced configuration.

Key Finding: Differential Stall Prediction Accuracy Between Configurations

The most significant result of this benchmark study is the striking difference in stall prediction accuracy between the reference and fenced turbine configurations. Figure 9 presents a summary comparison of the MAPE values, directly illustrating the superior predictive reliability of the stall-fenced configuration relative to the reference turbine.

Figure 9 shows a consistent pattern across all zones. The reference turbine achieves lower MAPE values in the pre-stall range (2.0% vs 7.5% for T*, pre-stall full), while the fenced turbine achieves much lower MAPE values in the post-stall zone (57.6% vs 325.6% for T*). In the full zone (φ=0.075-0.275), the fenced turbine MAPE of 18.6% for T* is far lower

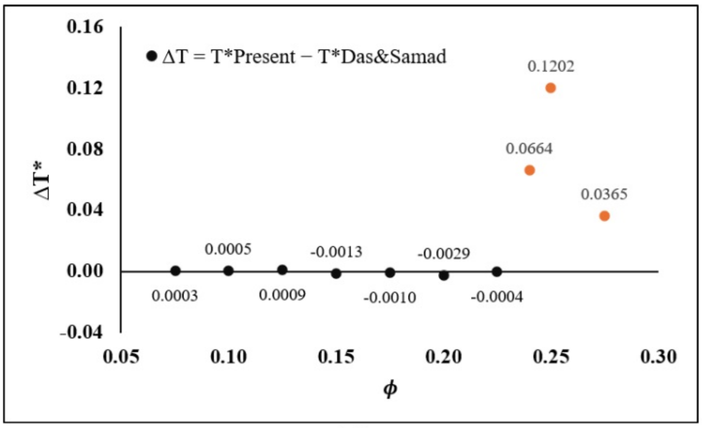

(a)

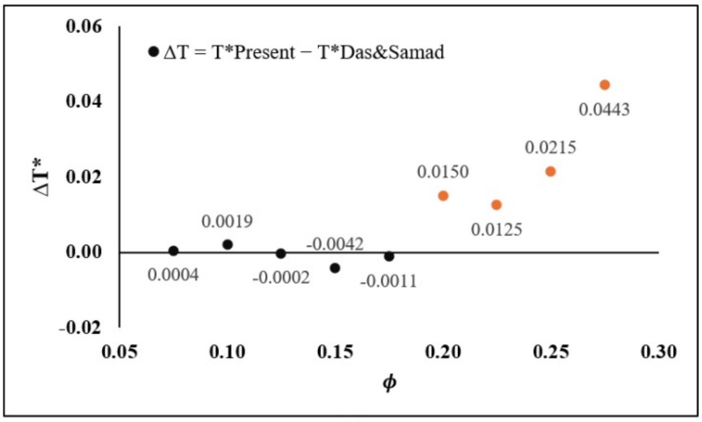

(b)

Note. Black markers indicate pre-stall data points ($\varphi \leq 0.225$ for the reference turbine; $\varphi \leq 0.250$ for the stall-fenced turbine) where steady RANS predictions are considered reliable. Orange markers indicate post-stall data points where RANS breakdown occurs; these points are excluded from MAPE calculations. The horizontal reference line at $\Delta T^* = 0$ denotes perfect agreement with Das & Samad (2020). The maximum post-stall deviation for the reference turbine is $\Delta T^* = 0.1202$ at $\varphi = 0.250$, compared to $\Delta^*T^{**} = 0.0443$ for the stall-fenced turbine at $\varphi = 0.275$, confirming the superior RANS predictive reliability of the fence-equipped geometry in the post-stall regime. Numerical data sourced from Das & Samad, Energy, 194, Article 116864 (https://doi.org/10.1016/j.energy.2019.116864)

Figure 8. Residual error scatter plot of non-dimensional torque (δt = t*present - t*Das&Samad) for (a) reference turbine and (b) stall-fenced turbine configurations across the full flow coefficient range φ = 0.075-0.275

than the reference turbine value of 73.9%, confirming the overall superior prediction accuracy of the RANS framework when applied to the fenced geometry across the entire operating range. The stall onset of the reference turbine exceeds φ=0.275 in the benchmark, whereas the stall of the fenced turbine is correctly reproduced at φ = 0.250.

This behavioral difference is explained through two complementary mechanisms. First, the stall characteristics are fundamentally different between the two configurations. In the reference turbine, the stall is sudden and large-scale, driven by leading-edge boundary-layer separation. While the general aerodynamic behavior of Wells turbines is stable with negligible dynamic effects, making steady simulations fundamentally adequate for overall performance evaluation (Ghisu et al., 2018), predicting the exact onset of stall on a clean blade remains inherently difficult for steady RANS. Because the absence of geometric disturbance on the clean blade means the model lacks an explicit physical feature to trigger surface stall, steady RANS often struggles to accurately resolve the boundary-layer separation point. In the fenced turbine, the stall fence introduces a discrete local vorticity structure that forces a geometry-driven separation mechanism, resulting in an early stall triggered by geometry rather than by smooth boundary-layer dynamics. Steady RANS is better able to capture such geometry-induced flow features, as evidenced by the near-zero stall-point deviation. The contrasting prediction accuracy between the two

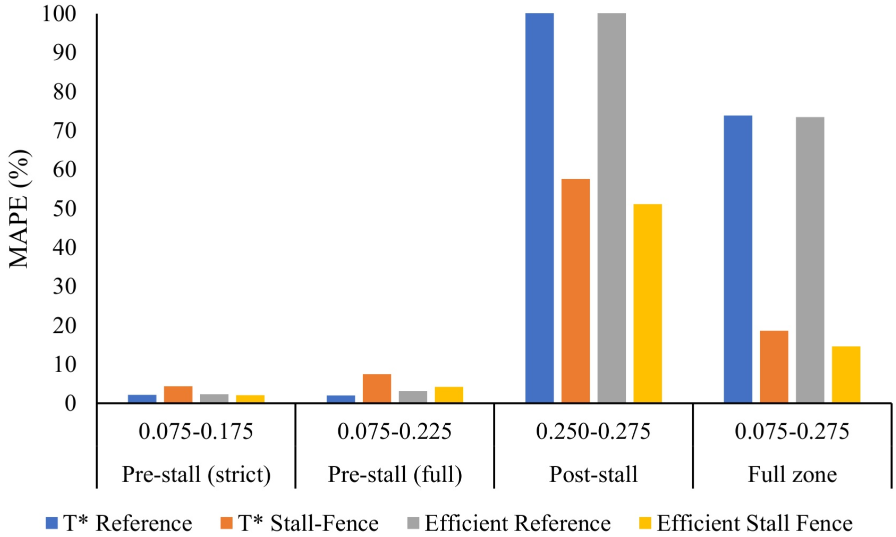

Note. MAPE values are computed as the mean absolute percentage deviation of the current benchmark results from the numerical data reported by Das & Samad (2020). Four flow zones are presented: pre-stall strict (φ = 0.075-0.175), pre-stall full (φ = 0.075-0.225), post-stall (φ = 0.250-0.275), and full operating range (φ = 0.075-0.275). Post-stall MAPE values for the reference turbine (T* = 325.6%; η = 319.6%) exceed the chart axis maximum of 100% and are therefore represented by bars truncated at the axis limit; actual values are reported in Table 3. The post-stall zone is shaded to indicate the operating range where the predictive validity of steady RANS breaks down. All simulations were performed using ANSYS CFX 2022 R1 with the SST k-ω turbulence model.

Figure 9. Grouped bar chart of mean absolute percentage error (mape) for non-dimensional torque t* and efficiency η across flow zones for reference and stall-fenced turbine configurations

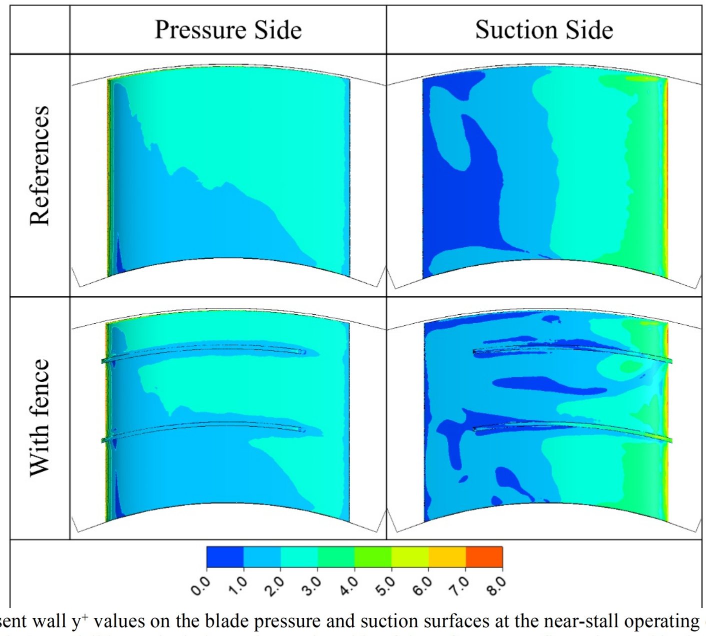

Note. Color contours represent wall y^+ values on the blade pressure and suction surfaces at the near-stall operating condition φ = 0.225. Although localized regions of elevated y^+ are visible particularly on the suction side of the reference configuration and in the vicinity of the fence attachment lines in the stall-fenced configuration, the area-weighted average y^+ remains below the threshold recommended for the SST k-ω turbulence model with low-Reynolds wall treatment ($y^+ \leq 1$ for the first prism layer). The elevated y^+ regions on the stall-fenced suction side correspond to the fence-induced vortex interaction zones at 40% and 80% span, where local flow acceleration increases near-wall velocity gradients. These localized exceedances do not compromise the overall near-wall resolution adequacy of the selected mesh. Results visualized using ANSYS CFD-Post 2022 R1.

Figure 10. Wall y^+ distribution on the blade pressure side and suction side for reference (top row) and stall-fenced (bottom row) turbine configurations at φ = 0.225

configurations, steady RANS failing to pinpoint the exact stall point in the reference turbine while successfully reproducing it in the fenced turbine, is itself indirect numerical evidence consistent with the smooth versus geometry-driven stall distinction described above.

Second, the fence geometry requires local mesh refinement in the critical regions along the blade at 40% and 80% of the span, which indirectly increases the near-wall resolution in those areas, as evidenced in Figure 10 by the tighter y^+ banding around the fence relative to the surrounding blade surface. This refinement improves the model's sensitivity to adverse pressure gradients near fence locations, facilitating earlier and more accurate detection of the geometry-driven separation responsible for the fenced turbine's superior stall-point and post-stall accuracy. This benefit, however, is confined to the separation-prediction regime and does not extend uniformly across the operating range. Further observation of Figure 9 shows that the reference turbine achieves better pre-stall accuracy (MAPE 2.0%) than the fenced configuration (MAPE 7.5%). This is physically consistent: the clean reference blade offers the most favorable conditions for steady RANS, without geometric disturbance or local vorticity interactions. The fence improves stall prediction accuracy at the cost of a slight reduction in pre-stall accuracy, an inherent trade-off in the interaction between fence-induced flow complexity and the steady RANS framework.

Physical Evidence of Flow Reproduction

To ensure that this benchmark model reproduces not only the integral performance parameters but also the underlying flow physics, a qualitative and semi-quantitative flow analysis is presented. This analysis corresponds to Figure 11 and Figure 12.

As seen in Figure 10, across all flow conditions, the reference turbine exhibits regular streamlines, with the flow largely attached to the suction surface. The presence of a small vortex region on the hub side at the lower part of the blade is consistent with the early development of secondary flow near the hub at high angles of attack. In the figure, there is no significant difference among the three conditions. At the flow-condition $\varphi=0.175$, the flow remains attached within the blade boundary layer. The conditions $\varphi=0.225$ and $\varphi=0.250$ show the same result. This is related to the non-dimensional torque, which continues to rise without any signs of near-stall, with no vortex appearing and no clearly defined reverse flow. The main reason the torque keeps rising in this benchmark is the failure of steady RANS to capture the recirculation zone, which forces the flow to remain attached even when inefficient. By contrast, in Figure 11 for the fenced case, the fence geometry requires a finer mesh to capture signs of separation, so the numerical result is clearer even though the error is relatively high.

Streamlines on the constant-radius planes at 40% and 80% of the blade span show a similar pattern; the flow in Figure 12 for the reference blade shows no vortex or separation point at which stall begins. Vortex reattachment is visible in the fenced configuration at the 40% and 80% spans, and the tip-leakage vortex is consistently captured. Therefore, the numerical simulation is able to capture the stall of the fenced blade at $\varphi=0.250$ even though its torque does not exactly match that of Das & Samad (2020).

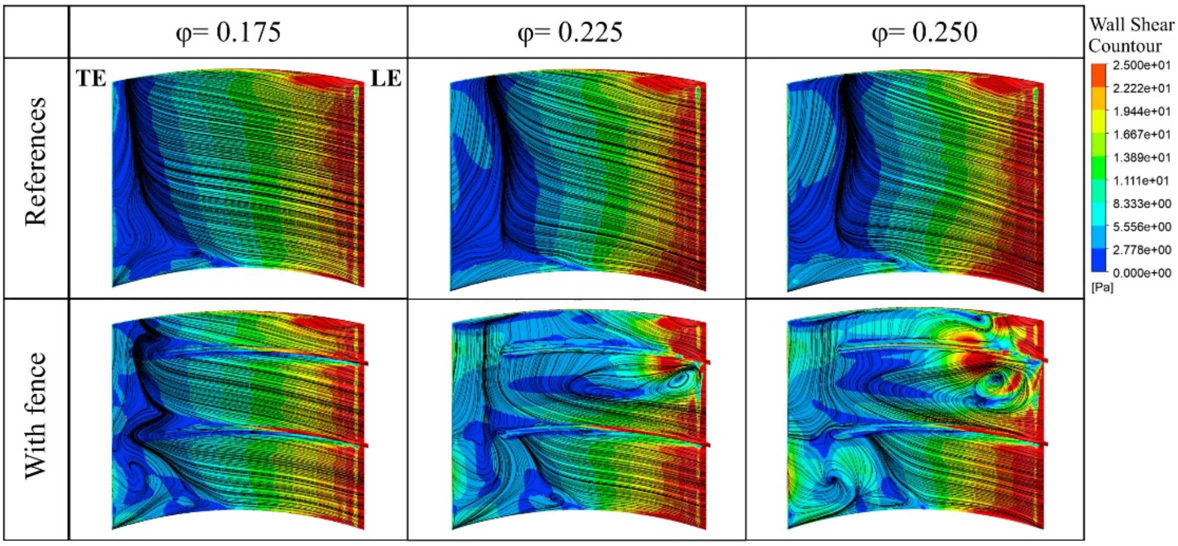

Note. Color contours represent wall shear stress magnitude τ_w (Pa) on the blade suction surface, with red indicating high shear stress (attached flow) and blue indicating low shear stress (flow separation or incipient stall). Overlaid black lines represent skin-friction lines derived from the wall-shear-stress vector field. The stall fence locations at 40% and 80% of the span are visible as red vertical markers in the bottom-row panels. Results obtained from steady-state RANS simulations using the SST k-ω turbulence model in ANSYS CFD-Post 2022 R1. TE = trailing edge; LE = leading edge.

Figure 11. Wall shear stress distribution and skin friction lines on the blade suction surface for reference (top row) and stall-fenced (bottom row) turbine configurations at φ = 0.175, 0.225, and 0.250

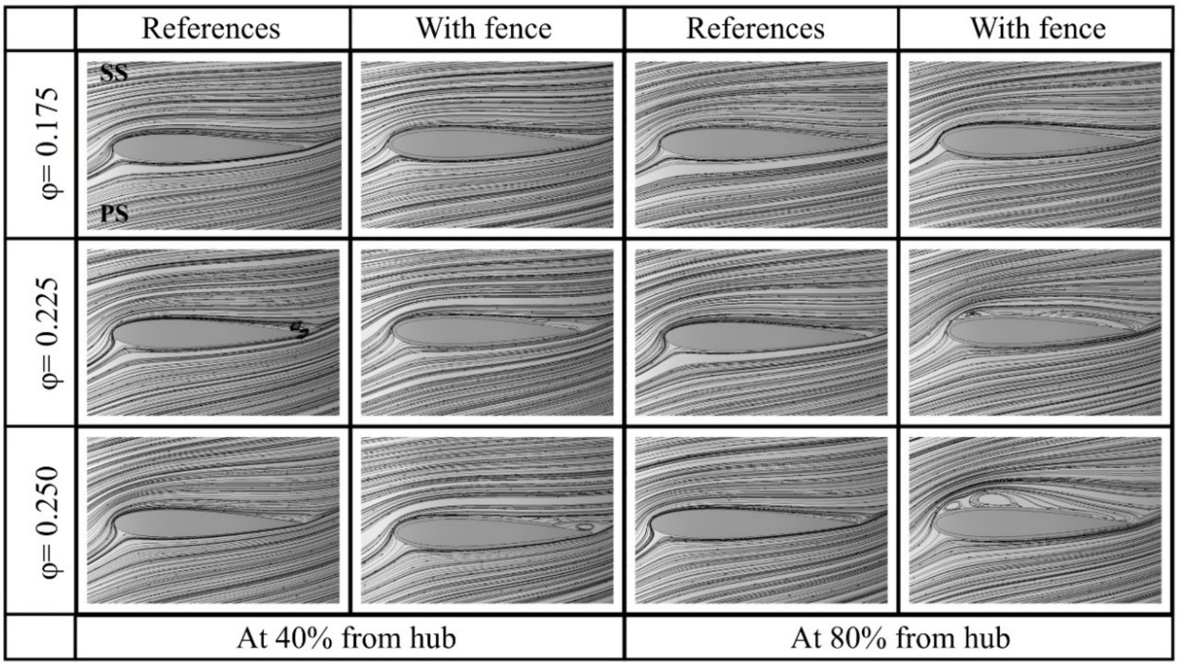

Note. Streamlines visualized on spanwise cross-sectional planes at 40% and 80% span measured from the hub, corresponding to the stall fence installation locations in the fenced configuration. Grey shaded regions indicate recirculation zones associated with boundary-layer separation on the blade suction surface. SS = suction side; PS = pressure side. Results obtained from steady-state RANS simulations using the SST k-ω turbulence model in ANSYS CFD-Post 2022 R1. The absence of a recirculation zone in the stall-fenced panels at $\varphi = 0.250$, compared with the reference configuration, demonstrates fence-induced suppression of leading-edge separation at the stall point.

Figure 12. Spanwise cross-sectional streamlines for reference and stall-fenced turbine configurations at 40% and 80% span locations and $\varphi = 0.175$, 0.225, and 0.250

Limitations of Steady RANS and Practical Implications

The results of this study confirm and quantify the inherent limitation of the steady RANS method in predicting stall onset for the reference Wells turbine geometry, while demonstrating its suitability for the fenced configuration. The overprediction increases from *142.6%* to *508.6%* in the post-stall region for the reference turbine, caused by three compounding mechanisms inherent to RANS formulation. First, the time-averaging procedure inherently smooths out the flow field, preventing the steady model from accurately resolving the sudden, geometry-independent onset of boundary-layer separation on a clean blade. Second, the SST k-ω production term artificially sustains near-wall momentum by overproducing turbulent kinetic energy in stagnation regions at the blade leading edge, thereby delaying the predicted separation onset beyond its true physical location. Third, the shear stress limiter embedded in the SST k-ω formulation which caps the turbulent shear stress at a value proportional to the turbulent kinetic energy via the relation $\tau_t \leq \rho a_1 k / \max(a_1\omega, \Omega F_2)$, where $a_1 = 0.31$ is the Bradshaw constant, Ω is the vorticity magnitude, and F_2 is a blending function is designed to prevent overprediction of eddy viscosity in adverse pressure gradient flows. However, in the near-stall regime of the Wells turbine suction surface, this limiter paradoxically retards the growth of turbulent eddy viscosity in the adverse-pressure-gradient region along the blade suction side, thereby sustaining artificial boundary-layer attachment beyond the true physical stall point. The limiter effectively reduces the momentum deficit that would otherwise trigger separation, causing the model to predict attached flow even after the physical boundary layer has detached. This mechanism, combined with the steady-state assumption that prevents the resolution of unsteady post-stall phenomena, including vortex shedding and dynamic reattachment cycles, collectively explains the severe torque overprediction of up to 508% at $\varphi = 0.275$. This observation is consistent with Gareev (2011) and the discrepancy acknowledged in Das & Samad (2020).

Despite this limitation, steady-state RANS provides fully adequate accuracy for engineering design within the pre-stall operating range. The MAPE of 2.0% for T* at φ=0.075-0.225 supports design decisions concerning geometry, operating conditions, and performance prediction within the practically relevant range for OWC applications. Higher-fidelity methods such as URANS, SAS-SST, or

LES are justified only when accurate post-stall flow physics are specifically required. For the fenced configuration, steady RANS proves effective as a predictive tool across the entire operating range, including the stall point. The use of a stall fence not only improves turbine performance but also enhances the predictive reliability of the steady RANS framework. This finding has direct practical implications for the CFD-based design of Wells turbines with passive flow control devices.

■ CONCLUSIONS

This study successfully demonstrates that independent CFD benchmark replication of Wells turbine performance, both with and without stall fences, is achievable using steady RANS with the SST k-ω turbulence model in ANSYS CFX, yielding pre-stall MAPE values of 2.0% and 4.4% for the reference and fenced configurations, respectively. These results confirm that the computational methodology of Das & Samad (2020) is numerically reproducible and solver-independent. A key finding of this benchmark is the fundamentally different stall-prediction behavior between the two configurations: steady-RANS fails to capture stall onset in the reference turbine, with post-stall torque overpredicted by up to 508%, whereas stall onset in the fenced turbine is reproduced with near-zero deviation at . This differential accuracy is explained by the nature of stall mechanisms; the progressive and transient leading-edge separation in the reference turbine is inherently beyond the predictive capability of steady averaging, whereas the geometry-driven vorticity imposed by the fence provides a discrete flow-separation trigger that steady RANS can resolve. Beyond performance validation, this study establishes that passive stall fences enhance not only turbine operating range but also the reliability of CFD-based design prediction, making steady RANS a more effective tool when applied to fence-equipped geometries. All findings reported here are valid within the operating conditions of the present simulation: a chord-based Reynolds number of $Re_c=4.3\times10^5$-4.5×10^5, corresponding to a rotational speed of *2000 rpm*, a chord length of $c=0.125$ *m*, and flow coefficients of φ=0.075-0.275 under standard air conditions. Within this Reynolds number regime, the flow is fully turbulent, and the SST k-ω model operates within its validated range. Extrapolation of these findings to significantly different Reynolds number regimes, such as full-scale OWC prototype conditions where Rec may exceed 10^6, should be approached with caution and would require independent validation. For engineering design purposes. Steady RANS is fully adequate within the pre-stall operating range for both configurations. At the same time, higher-fidelity methods such as URANS or LES remain necessary only when accurate post-stall physics are required. The validated numerical baseline presented here provides a transparent foundation for future parametric optimization of Wells turbines incorporating passive flow-control devices.

■ ACKNOWLEDGMENT

This work was supported by the RKAT PTNBH Universitas Sebelas Maret Year 2026, under the Research Scheme of “Penelitian Kolaborasi Internasional Top 100 (iTOP-100 UNS) Batch 2” with research grant/contract no. 973.1/UN27.22/PT.01.03/2026. The authors highly acknowledge this support.

■ DECLARATION OF GENERATIVE AI

During the drafting of this manuscript, the authors used Grammarly to refine sentence structure and improve scientific writing. Following the use of this tool, the author(s) reviewed and revised the content as necessary and accept full responsibility for the final content of the article.

■ REFERENCES

ANSYS, Inc. (2009). ANSYS CFX-solver theory guide (Release 12.1). ANSYS, Inc.

Curran, R., & Gato, L. M. C. (1997). The energy conversion performance of several types of Wells turbine designs. Proceedings of the Institution of Mechanical Engineers, Part A: Journal of Power and Energy, 211(2), 133–145. https://doi.org/10.1243/0957650971537051

Das, T. K., & Samad, A. (2020). Influence of stall fences on the performance of Wells turbine. Energy, 194, Article 116864. https://doi.org/10.1016/j.energy.2019.116864

Falcão, A. F. O., & Henriques, J. C. C. (2016). Oscillating-water-column wave energy converters and air turbines: A review. Renewable Energy, 85, 1391–1424. https://doi.org/10.1016/j.renene.2015.07.086

Gareev, A. (2011). Analysis of variable pitch air turbines for oscillating water column (OWC) wave energy converters [Doctoral dissertation, University of Wollongong]. University of Wollongong Research Online. https://ro.uow.edu.au/articles/thesis/Analysis_of_variable_pitch_air_turbines_ for_oscillating_water_column_OWC_wave_energy_converters/27664317

Ghisu, T., Puddu, P., & Cambuli, F. (2016). Physical explanation of the hysteresis in Wells turbines: A critical reconsideration. Journal of Fluids Engineering, 138(11), Article 111105. https://doi.org/10.1115/1.4033320

Ghisu, T., Cambuli, F., Puddu, P., Mandas, N., Seshadri, P., & Parks, G. T. (2018). Numerical evaluation of entropy generation in isolated airfoils and Wells turbines. Meccanica, 53(14), 3437–3456. https://doi.org/10.1007/s11012-018-0896-1

Halder, P., Mohamed, M. H., & Samad, A. (2018). Wave energy conversion: Design and shape optimization. Ocean Engineering, 150, 337–351. https://doi.org/10.1016/j.oceaneng.2017.12.072

Halder, P., Samad, A., Kim, J.-H., & Choi, Y.-S. (2015). High performance ocean energy harvesting turbine design–A new casing treatment scheme. Energy, 86, 219–231. https://doi.org/10.1016/j.energy.2015.03.131

Kumar, P. M., Halder, P., Husain, A., & Samad, A. (2019). Performance enhancement of Wells turbine: Combined radiused edge blade tip, static extended trailing edge, and variable thickness modifications. Ocean Engineering, 185, 47–58. https://doi.org/10.1016/j.oceaneng.2019.05.041

Menter, F. R. (1993). Zonal two-equation k-ω turbulence models for aerodynamic flows. In AIAA Fluid Dynamics Conference (AIAA Paper 93-2906). American Institute of Aeronautics and Astronautics. https://doi.org/10.2514/6.1993-2906

Okuhara, S., Takao, M., Takami, A., & Setoguchi, T. (2013). Wells turbine for wave energy conversion—Improvement of the performance by means of impulse turbine for bi-directional flow. Open Journal of Fluid Dynamics, 3(2A), 36–41. https://doi.org/10.4236/ojfd.2013.32A006

Setoguchi, T., Takao, M., & Kaneko, K. (1998). Hysteresis on Wells turbine characteristics in reciprocating flow. International Journal of Rotating Machinery, 4(1), 17–24. https://doi.org/10.1155/S1023621X98000025

Solfelt, D. A., & Maple, R. C. (2008). CFD analysis of a T-38 wing fence. In 46th AIAA Aerospace Sciences Meeting and Exhibit (AIAA Paper 2008-331). American Institute of Aeronautics and Astronautics. https://doi.org/10.2514/6.2008-331

Takao, M., Takasaki, K., Okuhara, S., & Setoguchi, T. (2014). Wells turbine for wave energy conversion—Improvement of stall characteristics by the use of 3-dimensional blades. Journal of Fluid Science and Technology, 9(3), Article JFST0052. https://doi.org/10.1299/jfst.2014jfst0052

Uddin, M. N., Opoku, F., & Atkinson, M. (2024). Investigation of a modified Wells turbine for wave energy extraction. Energies, 17(15), Article 3638. https://doi.org/10.3390/en17153638

Wauters, J., Couckuyt, I., Knudde, N., Dhaene, T., & Degroote, J. (2020). Multi-objective optimization of a wing fence on an unmanned aerial vehicle using surrogate-derived gradients. Structural and Multidisciplinary Optimization, 61(1), 353–364. https://doi.org/10.1007/s00158-019-02364-x